1-1-2013

Unidirectional coupling of surface plasmons with ultra-broadband and wide-angle efficiency: potential applications in sensing

Kun Li

Feng Xiao
Edith Cowan University

Fan Lu

Kamal Alameh
Edith Cowan University

Anshi Xu

10.1088/1367-2630/15/11/113040
Li, K., Xiao, F. , Lu, F., Alameh, K. , & Xu, A. (2013). Unidirectional coupling of surface plasmons with ultra-broadband and wide-angle efficiency: Potential applications in sensing. New Journal of Physics, 15(Nov), Article 113040. Available here

Unidirectional coupling of surface plasmons with ultra-broadband and wide-angle efficiency: potential applications in sensing

2013 New J. Phys. 15 113040

(http://iopscience.iop.org/1367-2630/15/11/113040)

New Journal of Physics
The open access journal for physics

Unidirectional coupling of surface plasmons with ultra-broadband and wide-angle efficiency: potential applications in sensing

Kun Li[1], Feng Xiao[2], Fan Lu[1], Kamal Alameh[2] and Anshi Xu[1,3]

[1] State Key Laboratory of Advanced Optical Communication Systems and Networks, School of Electronics Engineering and Computer Science, Peking University, Beijing 100871, People's Republic of China

[2] WA Center of Excellence for MicroPhotonic System, Electron Science Research Institute, Edith Cowan University, Joondalup, WA 6027, Australia

E-mail: lyrxas@pku.edu.cn

New Journal of Physics **15** (2013) 113040 (13pp)
Received 18 July 2013
Published 19 November 2013
Online at http://www.njp.org/
doi:10.1088/1367-2630/15/11/113040

Abstract. A cascaded-grating coupling scheme for unidirectionally coupling and launching surface plasmons from free-space light with ultra-broadband and wide-angle efficiency is proposed and theoretically investigated, and the potential applications in sensing are discussed. The cascaded sub-gratings of different periods couple the incident light over a relatively wide wavelength and angular range into surface plasmon polaritons (SPPs). After traveling a short distance, the SPPs interact with the sensed medium, and then are coupled back into freely propagating light through the nanoslit in the metal film. By observing the changes of SPP-mediated light coupled out through the slit, broadband sensing is achieved. A quantitative theoretical model is developed for performance prediction and validated with aperiodic Fourier modal method. Proof-of-principle demonstrations show that the spectral

[3] Author to whom any correspondence should be addressed.

full-width-half-maximum reaches 400 nm and meanwhile the angular width is up to 25°, both of which are almost four times compared to the reference single-periodic gratings. A wavelength sensitivity as high as 852 nm RIU^{-1} (RIU, refractive index units) and a relative intensity change up to $\sim 5 \times 10^4\%$ RIU^{-1} are obtained.

Contents

1. Introduction

Surface plasmon polaritons (SPPs) have been attracting world-wide attention and present an enabling technology to bridge electronic and photonic phenomena on submicrometer scales [1]. With optical fields strongly confined to the metal surface, SPPs are extremely sensitive to changes in the dielectric properties of the materials (index of refraction) they propagate through. Due to this attractive property, in recent decades, there has been rapidly growing interest in the field of SPP-based sensing, which has been utilized extensively for biomedical diagnostics and immunoassays [2–4], and has recently become the subject of intense research for high-throughput, label-free and real-time analytical monitoring and measurements [5–7]. However, before achieving the full potential of surface plasmon technology, the issue of unidirectional broadband coupling and launching SPPs from freely propagating light over a wide angular spectrum needs to be solved. In particular, for biomedical and chemical sensing such as wide-view observing mixed green algae microscope slide [8], light scattering measurements for mature blood cells [9] and circulating tumor cell detection in peripheral blood [10], the light scattered by the analytes could impinge upon detectors in a wide angle range. Thus the angle of incidence as well as the operating wavelength is generally unpredictable. As a result, it is favorable for the *SPP* coupling structure which is used to collect scattered light into detectors or spectrometers to have broadband and wide angular response, providing opportunities for gathering wide-angle scattered signals from analytes over a broadband spectrum and allowing robustness against beam alignment. Moreover, the ability for fingerprinting analytes to operate over a broad spectral range is highly desirable, which enables spectroscopic detection of the refractive index of analytes as a function of wavelength.

Furthermore, the most common methodologies, consisting of periodic arrays of apertures, slits or indentations [11, 12], are highly efficient at coupling incident beams into propagating SPPs at a wavelength-specific angle; they are limited in both operating wavelength and angular ranges. This inherent limitation originates from the periodicity itself, satisfying resonant coupling conditions between free-space radiation and SPP modes over a relatively narrow spectral bandwidth and angular width. On the other hand, although a non-resonant structure, e.g. a single scattering ridge or slit in a metallic film [13, 14], can provide broadband or

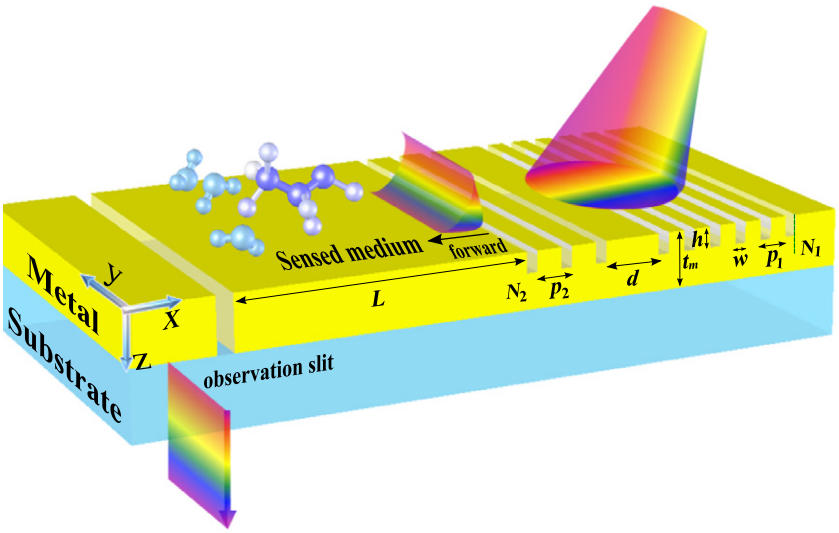

Figure 1. Schematic representation of the proposed ultra-broadband and wide-angle coupling and sensing scheme.

angle-insensitive free-space radiation to SPP modes coupling, it is not conducive to practical implementations due to relatively low efficiency. Recently, some of our authors demonstrated that cascading two silicon gratings that are of a proper angular interval between their peak efficiencies can lead to a wide flat-top angular coupling efficiency into dielectric waveguide [15]. While this silicon coupler has superior wide-angle performance, its bandwidth is somewhat limited due to a narrow operating wavelength ($\lambda = 1.55\,\mu$m) and the silicon-based composition is not suitable for broadband sensing. Also, fabrications of such triangular dielectric ridges and the realization of a compact footprint are considerable challenges. Consequently, unidirectional and broadband plasmonic couplers, with large acceptance angles required by the current broadband sensing, remain to be addressed.

In this paper, we propose a coupling and sensing scheme that uses two cascaded sub-gratings next to a nanoslit on a metal film for broadband and wide-angle SPPs excitation and refractive index measurement, as shown in figure 1. The structure is composed of two cascaded sub-gratings of different periods next to a nanoslit. The cascaded sub-gratings couple light over a broad wavelength and angular range into SPPs. Subsequently, the SPPs travel over a short distance where they can interact with biomolecules or a medium whose refractive index needs to be measured. Eventually, the transmitted SPPs are coupled back into light through a nanoslit through the metal film. Since the phase and amplitude of the SPPs are affected by the sensed medium, it causes intensity modulation of the light transmitted through the nanoslit, which can be measured to monitor the refractive index changes of the sensed medium. The two sub-gratings are cascaded to couple light over a broad wavelength and angular range into SPPs. Furthermore, the cascaded sub-gratings act as a broadband SPP launcher that excites multi-frequency SPPs, which after interacting with the sensed medium and coupling back into light through the nanoslit, generate interference fringes over a broad wavelength range. A quantitative theoretical model based on coupled-mode equations is developed for performance prediction and parameter engineering. The theoretical model is validated by comparing with fully vectorial

aperiodic Fourier modal method (a-FMM) [16] calculations. The spectral and angular coupling performance and sensing characterization will be analyzed and discussed.

2. Semi-analytical theoretical model

Figure 1 schematically illustrates the proposed ultra-broadband and wide-angle coupling structure illuminated by TM-polarized plane waves (magnetic field parallel to y-axis) for potential sensing applications. It is composed of two cascaded sub-gratings with feature width w and depth h next to a nanoslit with a separation L, milled in an optically thick metal film of thickness t_m evaporated onto a glass substrate. The sub-gratings are of structural distance d, and the first (or second) sub-grating is composed of N_1 (or N_2) features with period p_1 (or p_2). Here, the cascaded sub-gratings are modulated to function as a broadband and wide-angle SPP coupler, which enables operation over a broad spectral range, permits multispectral sensing schemes and alleviates the alignment.

Note that there are many geometrical features whose parameters are interlinked, so that pure simulations by varying all the important structural parameters are very time consuming and of excessive computational cost. Therefore, a quantitative theory with a clear physical picture is highly desirable. Some studies have theoretically investigated the coupling interactions to guide the design [17, 18]; however, little work has addressed the issue of cascaded-grating engineering. In this section, to circumvent this problem, we develop a semi-analytical theoretical model based on coupled-mode equations for the structure designed for any incidence/beaming angle θ and operating wavelength. The theory embodies all the key parameters, thus facilitating the structure design and elucidating the underlying physics.

For each sub-grating consisting of N periodic features, the excitation coefficients of SPPs may be expressed by recursive equations, referring to our previous work [19]:

$$\beta_N^- = \beta_1^- + t_1 u \frac{r_{N-1} u \beta_1^+ + w \beta_{N-1}^-}{1 - r_1 r_{N-1} u^2}, \tag{1a}$$

$$\beta_N^+ = w \beta_{N-1}^+ + t_{N-1} u \frac{\beta_1^+ + r_1 u w \beta_{N-1}^-}{1 - r_1 r_{N-1} u^2}, \tag{1b}$$

$$r_N = r_{N-1} + \frac{r_1 t_{N-1}^2 u^2}{1 - r_1 r_{N-1} u^2}, \tag{1c}$$

$$t_N = \frac{t_1 t_{N-1} u}{1 - r_1 r_{N-1} u^2}, \tag{1d}$$

where $u = \exp(\mathrm{i} k_0 n_{\mathrm{spp}} p_{1,2})$ and $w = \exp(\mathrm{i} k_0 p_{1,2} \sin\theta)$ with p_1 (or p_2) being the first (or second) sub-grating period. $\beta_1^{\pm}$, r_1 and t_1 are the backward- ('−') and forward-going ('+') SPPs excitation, reflection and transmission coefficients of a single feature, respectively. Since $\beta_N^{\pm}$, r_N and t_N are calculated recursively, starting from $\beta_1^{\pm}$, r_1 and t_1, the SPPs scattering coefficients calculation of a finite number of features is abridged to those of a single one, resulting in a great reduction of the computational cost.

To obtain a closed-form expression for the whole structure, we start from the elementary-event scattering coefficients of the cascaded grating and the nanoslit, as illustrated in figure 2: β_{g1}^- (or β_{g2}^-) and β_{g1}^+ (or β_{g2}^+) are the excitation coefficients of backward- and forward-going SPP modes by first (or second) sub-grating of N_1 (or N_2) features; β_s^- and β_s^+ are those by the

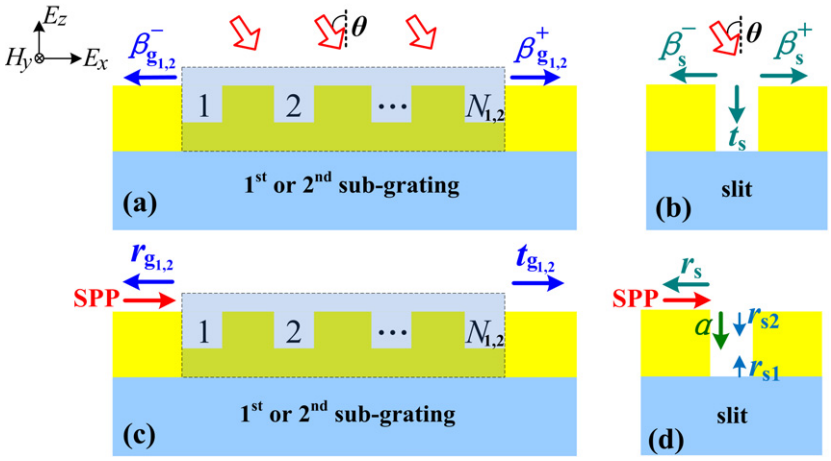

Figure 2. The involved main elementary scattering processes. They are all associated with the scattering of an electromagnetic field by a sub-grating (a, c) or a slit (b, d) under illumination of plane wave (a, b) and an SPP mode (c, d).

slit; r_{g1} (or r_{g2}) and t_{g1} (or t_{g2}) are the reflectance and transmittance coefficients of the first (or second) sub-grating; t_s is the excitation coefficient of the slit fundamental mode under plane wave illumination with amplitude I_0; α is the conversion coefficient from the SPP modes at the sensed medium–metal interface to the slit fundamental mode and vice versa; r_{s1} (or r_{s2}) and r_s are the reflectance coefficients of the slit fundamental mode at the bottom (or top) opening and of the SPP modes at the medium–metal interface, respectively.

Subsequently, the coupled-mode equations for the whole structure lead to:

$$\Psi_{g1}^{-} = \beta_{g1}^{-} I_0 + t_{g1} u_g \Psi_{g2}^{-}, \tag{2a}$$

$$\Psi_{g1}^{+} = \beta_{g1}^{+} I_0 + r_{g1} u_g \Psi_{g2}^{-}, \tag{2b}$$

$$\Psi_{g2}^{-} = w_g \beta_{g2}^{-} I_0 + r_{g2} u_g \Psi_{g1}^{+} + t_{g2} u_s \Psi_{s}^{-}, \tag{2c}$$

$$\Psi_{g2}^{+} = w_g \beta_{g2}^{+} I_0 + t_{g2} u_g \Psi_{g1}^{+} + r_{g2} u_s \Psi_{s}^{-}, \tag{2d}$$

$$\Psi_{s}^{-} = w_s \beta_{s}^{-} I_0 + r_s u_s \Psi_{g2}^{+} + \alpha v \Psi_{t}^{-}, \tag{2e}$$

$$\Psi_{t}^{-} = r_{s1} v \Psi_{t}^{+}, \tag{2f}$$

$$\Psi_{t}^{+} = t_s I_0 + \alpha u_s \Psi_{g2}^{+} + r_{s2} v \Psi_{t}^{-}, \tag{2g}$$

where $\Psi_{g1}^{\pm}$, $\Psi_{g2}^{\pm}$ and Ψ_{s}^{-} are complex amplitudes of magnetic field H_y of the backward- ('−') and forward-going ('+') SPP modes away from the first and the second sub-gratings and slit at the medium–metal interface, respectively; Ψ_{t}^{+} and Ψ_{t}^{-} are those of the slit fundamental modes propagating downward and upward, respectively. $u_g = \exp(ik_0 n_{spp} d)$ and $u_s = \exp(ik_0 n_{spp} L)$ with $n_{spp} = [n_d^2 n_m^2/(n_d^2 + n_m^2)]^{1/2}$ being the complex effective refractive index of the SPP modes at the medium–metal interface, and $v = \exp(ik_0 n_s t_m)$ with n_s being the complex effective refractive index of the slit fundamental mode. Note that the propagation losses of the SPPs have been embodied via complex n_{spp} and n_s. $w_g = \exp[ik_0(L_1 + d)\sin\theta]$ and $w_s = \exp[ik_0(L_1 + d + L_2 + L)\sin\theta]$ with $L_1 = \sum_1^{N_1-1} p_1 + w$ and $L_2 = \sum_1^{N_2-1} p_2 + w$ being the grating length of the

first and the second sub-grating, respectively, are the phase shifts introduced by the incident plane wave. This is because the zero phase of the incidence is assumed to be at the beginning of the first sub-grating for the calculation of $\beta_{g_1}^{\pm}$, $\beta_{g_2}^{\pm}$ and β_s^-.

In practice, $\beta_s^{\pm}$ can be omitted due to $|\beta_s^{\pm}| \ll |\beta_{g1}^{\pm}|$ and $|\beta_s^{\pm}| \ll |\beta_{g2}^{\pm}|$ for optimized sub-gratings. By neglecting trivial terms of high-order coupling coefficients, a closed-form expression for the transmission amplitude through the slit is obtained from equation (2)

$$\Psi_t^+ = \frac{I_0}{1 - r_{s1} r_{s2} v^2} \{ t_s + \frac{\alpha u_s}{1 - r_{g1} r_{g2} u_g^2 - r_s r_{g2} u_s^2} [t_{g2} u_g (\beta_{g1}^+ + r_{g1} u_g w_g \beta_{g2}^-) + (1 - r_{g1} r_{g2} u_g^2) w_g \beta_{g2}^+] \}. \tag{3}$$

The forward-going SPP modes excited by the cascaded sub-gratings are expressed as

$$\Psi_{g2}^+ = \frac{1}{1 - r_{g1} r_{g2} u_g^2 - r_s r_{g2} u_s^2} [t_{g2} u_g (\beta_{g1}^+ + r_{g1} u_g w_g \beta_{g2}^-) + (1 - r_{g1} r_{g2} u_g^2) w_g \beta_{g2}^+]. \tag{4}$$

The multiple reflections between the two sub-gratings (i.e. $r_{g1} r_{g2} u_g^2$), and those between the second sub-grating and the nanoslit (i.e. $r_{g2} r_s u_s^2$) can be neglected because of $|r_{g1} r_{g2} u_g^2| \ll 1$ and $|r_{g2} r_s u_s^2| \ll 1$. The term $t_{g2} u_g r_{g1} u_g w_g \beta_{g2}^-$, which means the SPPs excited backward by the second sub-grating and subsequently reflected by the first one, can also be ignored since the second sub-grating is unidirectionally designed (i.e. $|\beta_{g2}^-|^2 \ll |\beta_{g2}^+|^2$). As a result, equation (4) is reduced to

$$\Psi_{g2}^+ \approx t_{g2} u_g \beta_{g1}^+ + w_g \beta_{g2}^+. \tag{5}$$

Equation (5) interprets intuitively the interference between the forward-going SPPs by the transmission of the excitation of the first sub-grating and by the excitation of the second sub-grating. If β_{g1}^+ and β_{g2}^+ are designed properly with suitable spectral and angular intervals simultaneously between the comparable peak coupling coefficients, it is possible to obtain broad spectral full-width-half-maximum (FWHM) and angular width simultaneously, provided the structural distance d satisfies

$$\arg(t_{g2}) + k_0 \operatorname{Re}(n_{spp}) d - k_0 (\Sigma_1^{N_1 - 1} p_1 + w + d) \sin\theta) \approx 2 m\pi, \tag{6}$$

where the functions 'arg' and 'Re' refer to the argument and the real part, respectively, and m is an integer.

Similarly, the transmission amplitude through the observation slit is expressed as

$$\Psi_t^+ \approx \frac{I_0}{1 - r_{s1} r_{s2} v^2} (t_s + \alpha t_{g2} u_g u_s \beta_{g1}^+ + \alpha u_s w_g \beta_{g2}^+). \tag{7}$$

The physical interpretation of equation (7) is intuitively meaningful: the total transmitted intensity through the slit to detectors or spectrometers results from the interference between the SPP modes generated by the cascaded gratings (a composition of first sub-grating $\alpha t_{g2} u_g u_s I_0 \beta_{g1}^+$ and second sub-grating $\alpha u_s w_g I_0 \beta_{g2}^+$) and those by incidence light $I_0 t_s$. β_{g1}^+, β_{g2}^+ and t_{g2} can be calculated recursively from $\beta_1^{\pm}$ and t_1 by equation (1), thus the geometry engineering and the spectra calculation for N features are reduced into that for a single one. According to this equation, the SPP-mediated transmitted intensity depends on the phase shift terms $u_g u_s$ and $u_s w_g$, which are modulated by the refractive index changes. Therefore, by cascading two sub-gratings to unidirectionally couple SPPs from free-space light into the slit over a broadband and wide angular spectrum, we expect that broadband sensing will be achieved.

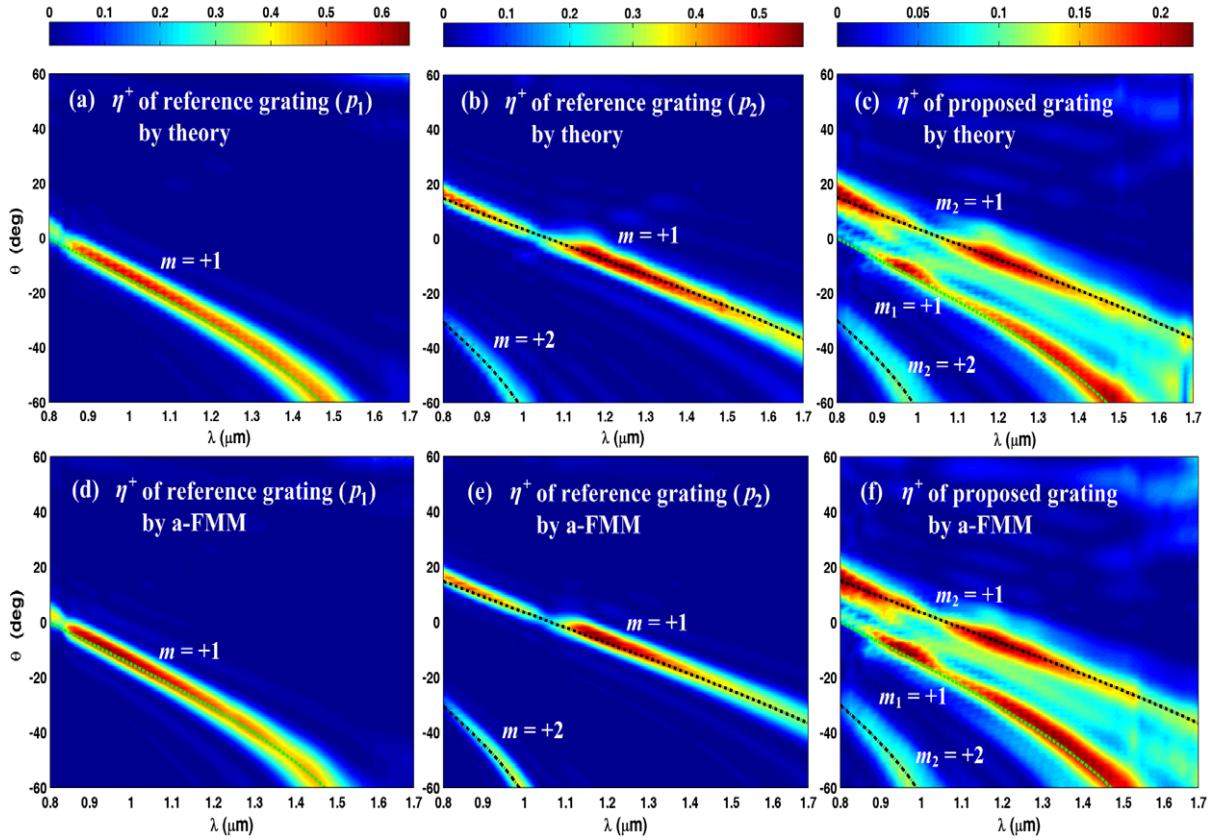

Figure 3. Comparisons between the spectral and angular coupling efficiency η^+ of the reference gratings of period p_1 (left panel) or p_2 (middle panel) and the proposed cascaded grating (right panel) predicted by the theoretical model (a)–(c) and calculated by a-FMM (d)–(f). The green line and the black line represent the respective grating equations of the first and the second reference gratings, with m being an integer related to the mth diffracted order. The calculations are performed with $w = 430$, $h = 100$, $p_1 = 785$ nm, $N_1 = 5$, $p_2 = 1052$ nm, $N_2 = 4$, $d = 440$ nm.

3. Results and discussions

Throughout this paper, the grating features are of constant depth $h = 100$ nm and width $w = 430$ nm, which greatly facilitates the manufacturing. With the theory, the periods and numbers of the first and the second sub-gratings are designed to be ($p_1 = 785$ nm, $N_1 = 5$) and ($p_2 = 1052$ nm, $N_2 = 4$), respectively, and the structural distance between the sub-gratings is set as $d = 440$ nm. Gold ($t_m = 300$ nm) with frequency-dependent permittivities tabulated in [20] is used as the metal film.

For an incident plane wave with a unit Poynting vector, we adopt the coupling efficiency $\eta^+ = |\Psi^+_{g2}|^2/D$ with D being the grating cross section to evaluate the coupling performance. Specifically, η^+ represents the ratio of forward-going SPPs power flow to the incident power flow that launches onto the grating [13]. Figure 3 shows the comparisons among the coupling efficiency η^+ of the reference grating with the same number of features ($N_1 + N_2$) of period

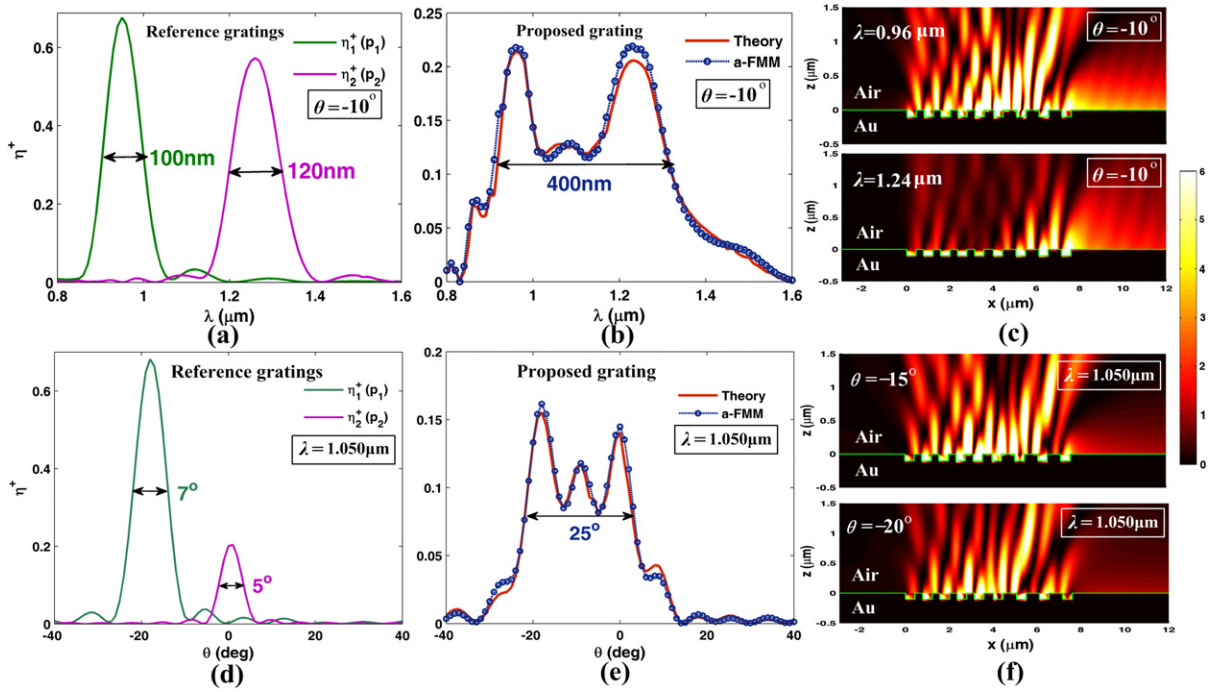

Figure 4. Comparisons between the spectral (a, b) and angular (d, e) coupling efficiency of the reference grating η_1^+ (or η_2^+) with $N_1 + N_2$ features of period p_1 (or p_2) (left panel), and the cascaded grating with N_1 features of period p_1, N_2 features of period p_2, and distance d between the sub-gratings (middle panel). Panels (c), (f) The scattered intensity $|H_y|^2$ for several wavelengths (c) or incidences (f) by finite element method.

$p_1 = 785$ nm (left panel) $p_2 = 1052$ nm (middle panel) and the proposed cascaded grating (right panel), predicted by the theoretical model (a)–(c) and calculated by a-FMM (d)–(f). As a result, simultaneous ultra-broadband and wide-angle coupling SPPs are achieved: the spectral FWHM reaches 400 nm covering a wide angular range from -10° to -60°, and meanwhile the angular width is up to 25° over an ultra-broad spectral range of 1–1.7 μm. Specifically, both the spectral FWHM and angular width of the proposed cascaded grating are broadened to nearly four times compared to the reference gratings, at an acceptable cost of decreasing the peak coupling efficacy only by a little over half. This is a novel property not possible in previous methodologies based on periodic-grating-coupling approaches where SPPs can only be launched at a specific wavelength and/or angle of incidence.

Figure 4 illustrates the comparison of spectral (a, b) and angular (d, e) performance between the reference grating of period p_1 (green line) or p_2 (magenta line) (left panel) and the proposed cascaded grating with theory predictions (red line) and the a-FMM data (blue-dashed line with circles) (middle panel) at a specific incidence angle $\theta = -10^\circ$ (a, b) or wavelength $\lambda = 1.050\,\mu$m (d, e). As shown in the figure, ultra-broadband and wide angular efficiency are realized in (b, e): the spectral FWHM is broadened from 100 or 120 to 400 nm and meanwhile the angular width is widened from 7° or 5° to 25°, nearly four times compared to the reference ones. Figures 4(c) and (f) depict the scattered SPPs intensity $|H_y|^2$ calculated by finite element method (FEM) at several wavelengths (c) or incidence angles (f), showing intuitively the

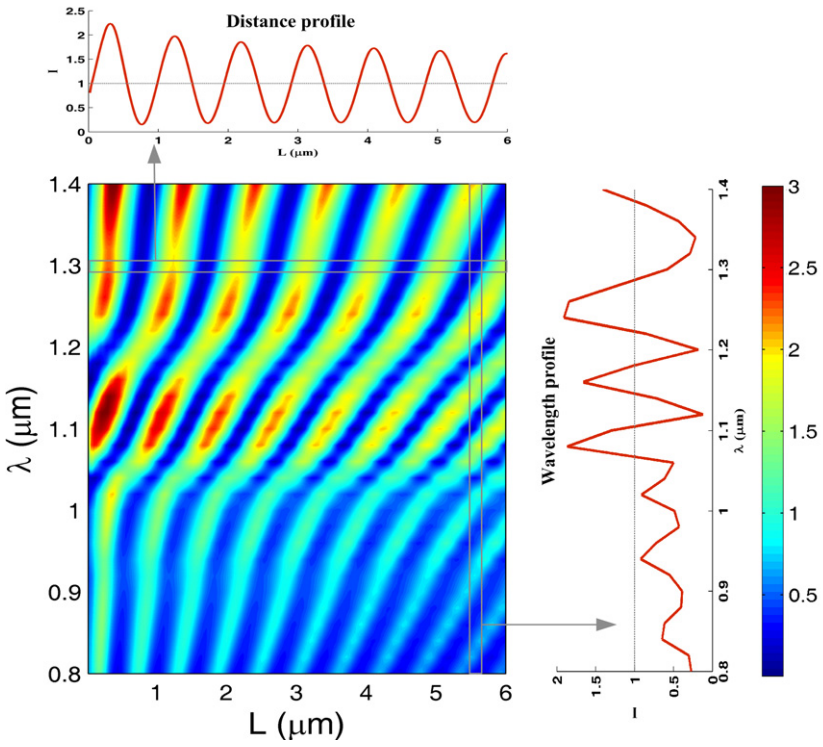

Figure 5. Normalized transmitted spectra as a function of grating–slit distance L (horizontal axis) and operating wavelength λ (vertical axis). Gray boxes indicate typical intensity plots obtained by horizontal or vertical cuts across this color map.

unidirectionally coupling free-space light into SPPs within the FWHMs. The accuracy of the theory has been quantitatively validated by comparing with a-FMM calculations, as illustrated in figures 3 and 4, where all the salient features of a-FMM calculations are quantitatively captured by the theory predictions. We emphasize that the theory is very efficient and flexible, since one only needs to scan $\beta_1^{\pm}$, r_1 and t_1 of a single feature instead of $\beta_N^{\pm}$, r_N and t_N of N features as functions of w and h. Subsequently, $\beta_N^{\pm}$, r_N and t_N can be calculated recursively starting from $\beta_1^{\pm}$, r_1 and t_1 with the recursive equations at negligible computational cost. Additionally, there are no restrictions on the features' geometry and refractive index profiles in the theory, making the theory versatile for various gratings.

Figure 5 shows a simulated color map of normalized transmission spectra as a function of grating–slit separation distance L (0.01–6.0 μm) and operating wavelength λ (0.8–1.4 μm) at a specific angle of incidence (the example of normal incidence was performed as a proof of concept). To achieve a normalized transmitted intensity spectrum, the intensity transmitted through the slit next to cascaded grating is divided by that of an isolated slit. The color of each point in the map corresponds to the normalized transmitted intensity with a specific combination of grating–slit distance (L) and wavelength (λ). The 'distance profile' (displayed by the horizontal gray box) reveals the dependence of intensity profile on the grating–slit distance L, for a specific incident wavelength. With the increase of L, the amplitudes of the interference oscillations are slightly smaller, indicating increased SPPs propagation loss at the

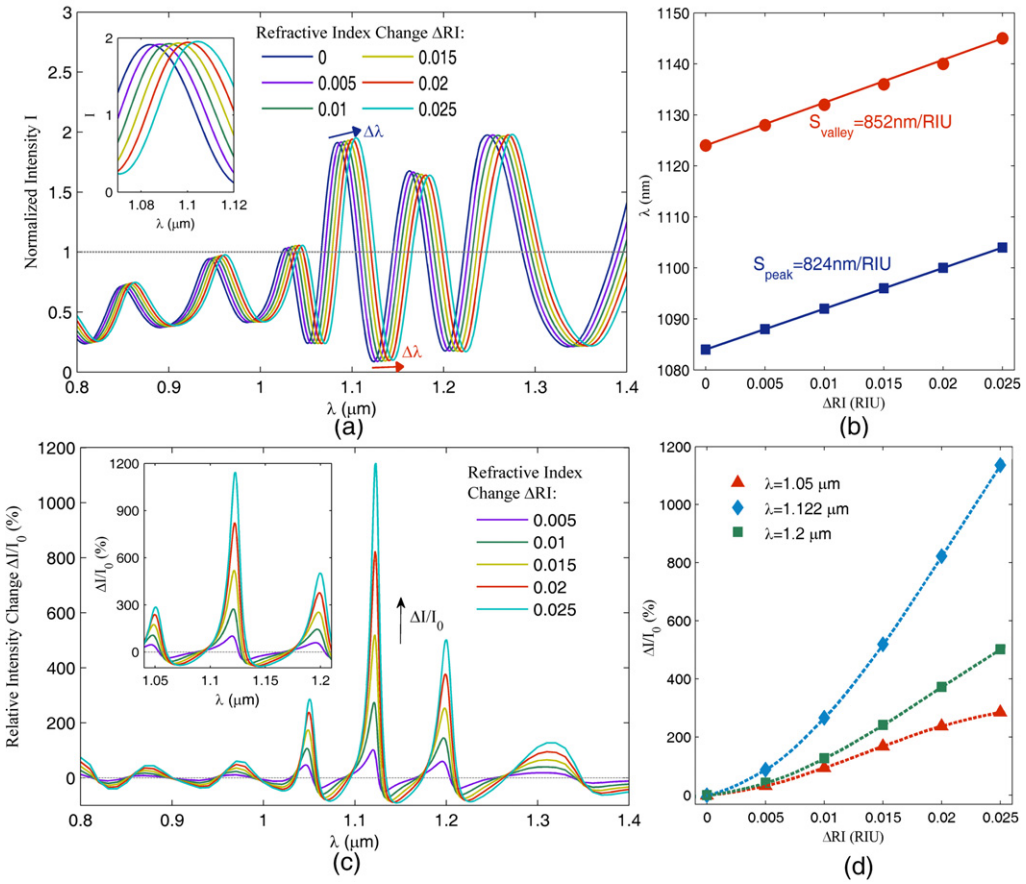

Figure 6. (a) Normalized transmitted intensity change versus the refractive index of the aqueous glycerol solution, where $\Delta n = 0$ indicates pure water ($n_{\text{water}} = 1.333$). (b) Spectral positions of the intensity peak (squares) and valley (dots) versus refractive index of the solutions. The solid lines are linear fits to the data. (c) Relative intensity changes as a function of wavelength (normalized to pure water) for the same structure. (d) Relative intensity change versus liquid refractive index for these three wavelengths.

medium–metal interface. From the 'wavelength profiles' (indicated by the vertical gray box), obvious interference patterns are displayed as a function of wavelength. With respect to larger L, a greater number of intensity peaks and valleys is observed, which suggests that the sensitivity may be further improved by moderately enlarging the grating–slit separation distance.

Since the phase and amplitude of SPPs from the cascaded grating can be affected by any analytes along their optical path because of an induced refractive index change, the final light transmitted through the slit contains information on the relative phase difference and amplitude of the different beams as we have stated in equation (7). As a result, by measuring the transmitted light intensity change caused by the presence of analytes as a function of wavelength, it is possible to retrieve the quantity of the sensed medium.

To illustrate the potential for sensing, grating–slit separation $L = 5.7\,\mu$m was chosen to detect glycerol concentrations in aqueous solutions as a proof-of-concept demonstration. Figure 6(a) illustrates the dependence of normalized transmitted intensity on the wavelength for

a series of glycerol–water solutions with different refractive indices. In practice, the refractive index of the aqueous solution can be enhanced by increasing the glycerol concentration [4]. It is clear that a vivid red-shift ($\Delta\lambda$) with the increase of liquid refractive index is observed at all incident wavelengths. The fringe shift is around $\Delta\lambda = 10$ nm for a refractive index change of $\Delta n = 0.01$. Using an optical spectrum analyzer of resolution 0.01 nm [21], the resolution of the proposed structure can be as high as $\Delta n_{\min} = 1 \times 10^{-5}$ refractive index unit (RIU). The peak and valley positions of the normalized intensity around 1085 and 1125 nm (indicated by the blue and red arrows, respectively) were measured as a function of the liquid refractive index and are plotted in figure 6(b). One can see that the positions of the peaks and the valleys vary approximately linearly with the refractive index of the aqueous glycerol solution. The refractive index sensitivities $S = \Delta\lambda/\Delta n$ are estimated to be 824 nm RIU^{-1} (peak) and 852 nm RIU^{-1} (valley) from the linear fits to the data. Figure 6(c) shows the relative intensity change $\Delta I/I_0 = (I_{\text{glycerol}} - I_0)/I_0 \times 100\%$, where I_{glycerol} means the transmitted intensity at a specific glycerol concentration, and I_0 represents that for pure water (i.e. zero glycerol concentration). The maximum relative intensity change is achieved at an incident wavelength of 1.122 μm with values up to 1137%. Similarly, dividing the difference in the relative intensity change $\Delta I/I_0$ by Δn, the figure of merit relative to the intensity change reaches $\sim 5 \times 10^4\%$ RIU^{-1} for 1.122 μm, as illustrated in figure 6(d). It is shown that at close but different wavelengths, the response can be drastically different, with higher sensitivity observed at 1.122 μm. In addition, under the illumination of other angles of incidence, similar transmitted interference fringes with shifted peak positions are obtained (not shown due to space limitation), depending upon whether constructive or destructive interference between the SPPs originating from cascaded grating and incident beam occurs.

Either monitoring the $\Delta\lambda$ or $\Delta I/I_0$, sensing is to measure the refractive index of solutions. In contrast to conventional approaches that utilize a specific excitation or resonant wavelength, such proposed sensing structure can operate over an ultra-broad spectral range, facilitating the selection of light sources and spectroscopic detection of the refractive index of the analytes. Note that, apart from the above-mentioned glycerol sensing in aqueous solution, the proposed sensor allows for fingerprinting of other analytes. These results may be of importance from both a theoretical point of view and for the broadband and wide angular surface plasmons coupling and launching, and refractive index detection in potential sensing.

4. Conclusions

In conclusion, we have proposed and theoretically investigated a cascaded-grating coupling scheme for unidirectionally coupling and launching SPPs from free-space light with simultaneously ultra-broadband and wide angular efficiency, and the potential applications in refractive index detection for sensing. A semi-analytical theoretical model has been developed to facilitate the design and predict the performance. Proof-of-principle demonstrations have shown that the spectral FWHM reaches 400 nm and the angular width is up to 25°, both of which are broadened to almost four times compared to the periodic reference grating, at an acceptable cost of decreasing peak coupling efficiency only by a little more than half. By monitoring the transmitted SPP-mediated light, refractive index detection with a high wavelength sensitivity of 852 nm RIU^{-1} and a relative intensity change up to $\sim 5 \times 10^4\%$ RIU^{-1} over a broad wavelength

range is achieved. The proposed coupling and sensing scheme may pave the way for applications in broadband and wide angular SPPs launching and sensing.

Acknowledgments

This work was supported by the Open Foundation of State Key Laboratory of Optical Communication Technologies and Networks (Wuhan Research Institute of Posts & Telecommunications), and by the State Key Laboratory of Advanced Optical Communication Systems and Networks, China.

References

[1] Baron A, Devaux E, Rodier J C, Hugonin J P, Rousseau E, Genet C, Ebbesen T W and Lalanne P 2011 Compact antenna for efficient and unidirectional launching and decoupling of surface plasmons *Nano Lett.* **11** 4207–12

[2] Gao Y, Xin Z, Gan Q, Cheng X and Bartoli F J 2013 Plasmonic interferometers for label-free multiplexed sensing *Opt. Express* **21** 5859–71

[3] Feng J, Siu V S, Roelke A, Mehta V, Rhieu S Y, Tayhas G, Palmore R and Pacifici D 2012 Nanoscale plasmonic interferometers for multispectral, high-throughput biochemical sensing *Nano Lett.* **12** 602–9

[4] Gao Y, Gan Q, Xin Z, Cheng X and Bartoli F J 2011 Plasmonic Mach–Zehnder interferometer for ultrasensitive on-chip biosensing *ACS Nano* **5** 9836–44

[5] Anker J N, Hall W P, Lyandres O, Shah N C, Zhao J and Van Duyne R P 2008 Biosensing with plasmonic nanosensors *Nature Mater.* **7** 442–53

[6] Stewart M E, Anderton C R, Thompson L B, Maria J, Gray S K, Rogers J A and Nuzzo R G 2008 Nanostructured plasmonic sensors *Chem. Rev.* **108** 494–521

[7] Lee K L, Lee C W, Wang W S and Wei P K 2007 Sensitive biosensor array using surface plasmon resonance on metallic nanoslits *J. Biomed. Opt.* **12** 044023

[8] Wu J, Zheng G, Li Z and Yang C 2011 Focal plane tuning in wide-field-of-view microscope with Talbot pattern illumination *Opt. Lett.* **36** 2179–81

[9] Su X, Kirkwood S E, Gupta M, Curtis L M, Qiu Y, Wieczorek A J, Rozmus W and Tsui Y Y 2011 Microscope-based label-free microfluidic cytometry *Opt. Express* **19** 387–98

[10] Nagrath S *et al* 2007 Isolation of rare circulating tumour cells in cancer patients by microchip technology *Nature* **450** 1235–39

[11] Egorov D, Dennis B S, Blumberg G and Haftel M I 2004 Two-dimensional control of surface plasmons and directional beaming from arrays of subwavelength apertures *Phys. Rev.* B **70** 033404

[12] Bonod N, Popov E, Li L and Chernov B 2007 Unidirectional excitation of surface plasmons by slanted gratings *Opt. Express* **15** 11427–32

[13] Liu H, Lalanne P, Yang X and Hugonin J P 2008 Surface plasmon generation by subwavelength isolated objects *IEEE J. Sel. Top. Quantum Electron.* **14** 1522–29

[14] Chen J, Li Z, Lei M, Yue S, Xiao J and Gong Q 2011 Broadband unidirectional generation of surface plasmon polaritons with dielectric-film-coated asymmetric single-slit *Opt. Express* **19** 26463–9

[15] Li K, Li G, Xiao F, Lu F, Wang Z and Xu A 2012 Unidirectionally optical coupling from free space into silicon waveguide with wide flat-top angular efficiency *Opt. Express* **20** 18545–54

[16] Silberstein E, Lalanne P, Hugonin J P and Cao Q 2001 On the use of grating theory in integrated optics *J. Opt. Soc. Am.* A **18** 2865–75

[17] Basha M A, Chaudhuri S and Safavi-Naeini S 2010 A study of coupling interactions in finite arbitrarily-shaped grooves in electromagnetic scattering problem *Opt. Express* **18** 2743–52

[18] Li G, Xiao F, Cai L, Alameh K and Xu A 2011 Theory of the scattering of light and surface plasmon polaritons by finite-size subwavelength metallic defects via field decomposition *New J. Phys.* **13** 073045

[19] Li G, Xiao F, Li K, Alameh K and Xu A 2012 Theory, figures of merit, and design recipe of the plasmonic structure composed of a nano-slit aperture surrounded by surface corrugations *J. Lightwave Technol.* **30** 2405–14

[20] Palik E D 1985 *Handbook of Optical Constants of Solids* (New York: Academic)

[21] Xiao F, Li G, Alameh K and Xu A 2013 Fabry–Perot-based surface plasmon resonance sensors *Opt. Lett.* **37** 4582–4